

Article

Kinetic Analysis of the Thermal Decomposition of a Synthetic Mercury Jarosite

Mizraim U. Flores ^{1,*}, Iván A. Reyes ^{2,3} , Elia G. Palacios ⁴ , Francisco Patiño ⁵, Julio C. Juárez ⁶ , Martín Reyes ⁶, Aislinn M. Teja ⁴, Hernán Islas ² and Emmanuel J. Gutiérrez ^{2,3}

¹ Área Electromecánica Industrial, Universidad Tecnológica de Tulancingo, Camino a Ahuehuetitla, 501, Col. Las Presas, Tulancingo, Hidalgo 43645, Mexico

² Instituto de Metalurgia, Universidad Autónoma de San Luis Potosí, San Luis Potosí, S.L.P. 78210, Mexico; iareyesdo@conacyt.mx (I.A.R.); islas_79hv@yahoo.com.mx (H.I.); ejgutierrezca@conacyt.mx (E.J.G.)

³ Catedrático CONACYT, Av. Insurgentes Sur 1582, Col. Crédito Constructor, Alcaldía Benito Juárez 03940, Mexico

⁴ Instituto Politécnico Nacional, DIMM-ESIQIE, UPALM, 07738 Ciudad de México, Mexico; epalacios@ipn.mx (E.G.P.); aislinn_teja@uaeh.edu.mx (A.M.T.)

⁵ Ingeniería en Energía, Universidad Politécnica Metropolitana de Hidalgo, Boulevard acceso a Tolcayuca 1009, Ex-Hacienda San Javier, Tolcayuca, Hidalgo 43860, Mexico; franciscopatinocardona@gmail.com

⁶ Área Académica de Ciencias de la Tierra y Materiales, Universidad Autónoma del Estado de Hidalgo, Carretera Pachuca–Tulancingo km 4.5, Mineral de la Reforma, Hidalgo C.P. 42184, Mexico; jcjuarez@uaeh.edu.mx (J.C.J.); mar_77_mx@hotmail.com (M.R.)

* Correspondence: mflores@utec-tgo.edu.mx or uri_fg@hotmail.com; Tel.: +527711433711

Received: 1 February 2019; Accepted: 22 March 2019; Published: 27 March 2019



Abstract: Jarosites are widely used in the hydrometallurgical industry of zinc to eliminate iron and other impurities contained in the concentrates. However, these compounds can also incorporate elements of significant environmental concern such as Ti^+ , Hg^{2+} , Pb^{2+} , Cd^{2+} , Cr(VI) , and As(V) . In this work, the characterization of a synthetic mercury jarosite and its thermal decomposition kinetics are reported. XRD and FTIR analyses confirm that a mercury jarosite— $\text{Hg}_{0.40}(\text{H}_3\text{O})_{0.2}\text{Fe}_{2.71}(\text{SO}_4)_{2.17}(\text{OH})_{4.79}(\text{H}_2\text{O})_{0.44}$ —was successfully synthesized. Four mass loss events were observed by thermogravimetric analysis at 290 °C, 365 °C, 543 °C, and 665 °C. The third event corresponds to mercury decomposition into mercury oxide, whilst the forth is related to the jarosite to hematite transformation determined by X-ray diffraction starting at around 600 °C. According to the kinetic parameters (activation energy and frequency factor) of the thermal decomposition process, the fourth stage required the highest energy ($E_a = 234.7 \text{ kJ}\cdot\text{mol}^{-1}$), which corresponds to elimination of sulfur and oxygen from the jarosite lattice. Results show that jarosite-type compounds have the capability to incorporate heavy metals into their structure, retaining them even at high temperatures. Therefore, they can be used as a remediation strategy for heavy metals, such as mercury and others elements of environmental concern.

Keywords: synthetic mercury jarosite; kinetics; thermal decomposition; activation energy; frequency factor

1. Introduction

Mercury is widely known for its high toxicity; in recent years, its concentration levels have increased in several environments [1–3]. Mercury pollution in water, fish, and humans has become of great concern worldwide, since it strongly affects human health and can seriously damage the nervous system.

Mercury-dependent artisanal and small-scale gold mining (ASGM) is the largest source of mercury pollution on Earth. Commonly, effluents are discharged in aquifers without treatment prior to mercury release [3,4]. High levels of mercury in water represent a serious environmental problem in countries like China, Spain, Brazil, the Czech Republic, and the United States [3–13].

Several techniques of mercury removal—including electrochemical methods, nanotechnology, phytoextraction, phytostabilization, zeolite filters, and sedimentation, among others—have been developed during the past decades, but they are not yet completely efficient because of the instability of this element after being treated [14–25].

Natural jarosite was discovered in 1852 in the south-eastern cliffs of Spain [26]. The importance of the formation and decomposition of jarosite-type compounds depends on its presence in the soils, sediments, and deposits where it is formed [27]. The family of jarosite compounds $[MFe_3(SO_4)_2(OH)_6]$ —where M can be Na^+ , K^+ , Ag^+ , Rb^+ , H_3O^+ , Tl^+ , NH_4^+ , Hg^{2+} or Pb^{2+} —has a wide range of applications in the metallurgical industry. The jarosite precipitation process is the most widespread technology in the zinc industry, used for iron removal from the hot-acid leaching solutions prior to recovery of zinc [28]. Jarosites have the capability to incorporate elements of environmental concern—such as Pb^{2+} , As(V), Cr(VI), Cd^{2+} , and even Hg^{2+} —into their structure. Patiño et al. 2013 a, 2013 b; Flores et al. 2012; Reyes et al. 2011; Asta et al. 2009 have conducted the most recent studies regarding the incorporation of arsenic into the structure of jarosite-type compounds under different conditions of pH, temperature, and particle size [29–33].

Dutrizac and Kaiman, 1976, were the first researchers to synthesize jarosite-type compounds with mercury, which was achieved by incorporation of 14.62 wt. % of mercury oxysulfate. Dutrizac and Chen, 1981, also synthesized jarosite-type compounds with mercury, although they incorporated only 0.08 wt. % of mercury. There are no reports in the literature regarding the stability of mercury jarosite compounds after being exposed to high temperatures [34,35].

The thermal decomposition of jarosite-type compounds containing K^+ , Na^+ , Pb^{2+} , H_3O^+ , and NH_4^+ was analyzed by Frost et al. 2005, 2006 a, 2006 b [36–38]. Three mass loss events were observed in Na^+ and K^+ jarosites; the first attributed to loss of water, the second associated with a dehydroxylation process, and the third related to transformation of sulfur compounds. In the case of jarosites containing Pb^{2+} , H_3O^+ , and NH_4^+ , four mass loss events were reported; the three stages described above and a fourth one attributed to the transformation of cationic sites (Na^+ , K^+ , Ag^+ , Rb^+ , H_3O^+ , Tl^+ , NH_4^+ , Hg^{2+} , or Pb^{2+}). In all cases, the complete decomposition of this compound was reached above 700 °C. None of the above-mentioned works used compounds containing elements of environmental importance such as mercury [36–38].

Therefore, the present work presents the thermal characterization and subsequent thermal decomposition kinetics of jarosite-type compounds containing mercury. The main objective was to investigate the high temperature behavior of this toxic element in order to propose its thermal decomposition stoichiometry.

2. Materials and Methods

2.1. Characterization

The synthesis of mercury jarosite was conducted according to the procedure reported by Ordoñez et al. [39], in which 1 L of a solution containing $0.27\text{ mol}\cdot\text{L}^{-1} Fe_2(SO_4)_3\cdot nH_2O$ and $0.58\text{ mol}\cdot\text{L}^{-1} Hg(NO_3)_2\cdot H_2O$ was kept at constant temperature of 93 °C under stirring (400 rpm) for 24 h in a Pyrex reactor. The obtained solids were vacuum filtered and rinsed with hot distilled water at 70 °C to remove excess reagents, and the precipitate was finally dried at 65 °C. Ultrapure deionized water (resistivity of $\approx 18.0\text{ M}\Omega\cdot\text{cm}$) and Sigma-Aldrich reagents in ACS grade were used for the synthesis of the mercury jarosite. Characterization by X-ray diffraction (XRD) was carried out in an Inel Equinox 2000 diffractometer (Thermo Fisher Scientific, Waltham, MA, USA); patterns were collected in the 2θ range 10–90°, acquisition time 10 s, Co K α 1 radiation ($\lambda = 1.78901\text{ \AA}$), 40 kV and 25 mA, using a

Curved Position Sensitive Detector and germanium monochromator. The 0.002° angular resolution of the diffracted beam was predefined by the channel size of $50\text{ }\mu\text{m}$, and the distance between sample and the detector equal to 1406.9 mm .

The approximate formula of the synthesized compound was calculated from elemental analysis by atomic absorption spectrometry (AAS, PerkinElmer Analyst 200, PerkinElmer Waltham, MA, USA), and prior digestion of a solid sample with hydrochloric acid (HCl, ACS reagent 37% Sigma-Aldrich, Saint Louis, MO, USA) to determine contents of Hg and Fe. The SO_4^{2-} was determined by gravimetric analysis from the BaSO_4 precipitation [40], and the O + H content was calculated as the weight difference. The Fourier transform infrared spectroscopy (FTIR) analysis was performed in a Perkin Elmer Frontier FT-IR spectrometer (PerkinElmer Waltham, MA, USA) in the mid-infrared region ($400\text{--}4000\text{ cm}^{-1}$). Thermal characterization was carried out by thermogravimetric and differential thermal analysis (TGA/DTA) in a TGA/DTA 851e Mettler-Toledo (Mettler-Toledo, Columbus, OH, USA). Experiments were conducted at $10\text{ }^\circ\text{C}\cdot\text{min}^{-1}$ heating rate under $666 \times 10^{-3}\text{ m}^3\cdot\text{min}^{-1}$ air flow.

2.2. Thermal Decomposition Kinetics

For the thermal decomposition kinetics, synthetic mercury jarosite samples (1 g) were subjected to 1 h isothermal treatments ($320, 400, 600$, and $700\text{ }^\circ\text{C}$) to determine the decomposition reactions, according to the identified mass loss events by TGA. SEM-EDS analyses—conducted in a JEOL JSM-6701F microscope (JEOL, Tokyo, Japan)—were carried out for each isothermally treated sample to obtain the elemental composition of the residues, and to be able to establish the possible reaction mechanism. The experimental values obtained at different temperatures for the time (t), at which the fraction transformed was $Y_{0.5}$, were used to estimate the activation energy (E_a) by the “time to given fraction” method.

3. Results and Discussion

3.1. Characterization

Figure 1 shows the XRD patterns of the synthesized compound. According to the International Center for Diffraction Data-Powder Diffraction Files, the solid was identified as synthetic mercury jarosite, $\text{Hg}_{0.5}\text{Fe}_3(\text{SO}_4)_2(\text{OH})_6$ (PDF 00-030-0837). No additional reflections are observed, indicating that a pure compound was obtained.

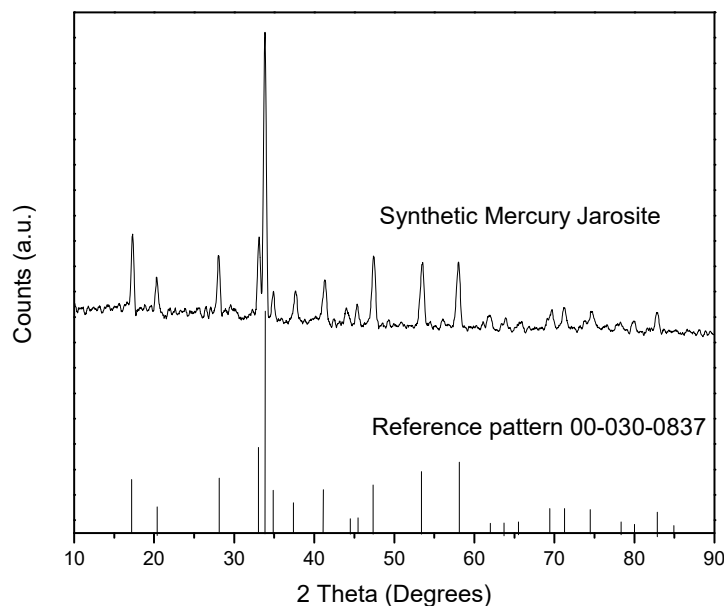


Figure 1. X-ray pattern corresponding to the synthesized solid; all of the reflections correspond to the synthetic mercury jarosite.

According to the chemical analysis presented in Table 1 and considering the following molar relationships: $2\text{Hg} + \text{H}_3\text{O} = 1$, $\text{Fe} = 3$, $\text{SO}_4 = 2$, and $\text{OH} = 1 + 3\text{Fe} - 2\text{SO}_4$, remaining wt. % is attributed to the presence of water in the structure (see FTIR results). The calculated approximate formula was $[\text{Hg}_{0.40}(\text{H}_3\text{O})_{0.2}]\text{Fe}_{2.71}(\text{SO}_4)_{2.17}(\text{OH})_{4.79}(\text{H}_2\text{O})_{0.44}$. The FTIR spectrum ($3500\text{--}400\text{ cm}^{-1}$) of the synthetic mercury jarosite is shown in Figure 2 and the results from the spectral analysis are listed in Table 2. According to the stoichiometric formula obtained from chemical analysis, bands due to sulfate ion, hydroxyl groups, and metal–oxygen bonds (Fe–O and Hg–O) are expected in the IR spectrum. Regarding the $\nu(\text{M}-\text{O})$ stretching vibrations, two bands were reported for pure HgO : the asymmetric mode observed at 600 cm^{-1} and the symmetric mode at 470 cm^{-1} or 484 cm^{-1} [41,42]. Shifting of both bands to 618 cm^{-1} and 476 cm^{-1} , respectively, relate to incorporation of the carbonate group into the mercury oxide structure [42].

Table 1. Elemental analysis of the obtained products.

Species	wt. %	Analysis Technique
Fe	26.9	AAS
SO_4	37.1	Gravimetric
Hg	14.1	AAS
$\text{OH} + \text{H}_3\text{O} + \text{H}_2\text{O}$	21.9	Difference

The sharp band in Figure 2 present at 617 cm^{-1} was attributed to the $\nu(\text{Hg}-\text{O})$ stretching vibration, whilst the shoulder at 490 cm^{-1} and the peak at 463 cm^{-1} could correspond to both the Hg–O and the Fe–O covalent bonding, confirming the structural incorporation of mercury [42–45]. The six vibration modes (two ν_3 , two ν_4 , one ν_1 , and one ν_2) due to C_{3v} sulfate anion in the jarosite structure can be clearly identified in the spectrum [42]. Bands at 1184 cm^{-1} and 1087 cm^{-1} relate to the asymmetric stretching mode (ν_3), and those observed at 671 cm^{-1} and 636 cm^{-1} to the ν_4 asymmetric bending vibration. The band observed at 430 cm^{-1} is associated with the symmetric bending mode (ν_2), and the symmetric stretching (ν_1) vibration appear as a shoulder at 996 cm^{-1} , which is overlapped with the strong band at 1004 cm^{-1} , corresponding to the in-plane bending mode of the hydroxyl group [42,43].

Additionally, the band at 1630 cm^{-1} corresponds to the bending vibration of water molecules, often present in synthetic samples where H_3O^+ replaces some of the monovalent sites [45]. Finally, the broad peak centered at 3310 cm^{-1} confirms the presence of OH^- and H_2O in the molecule, and the broad peaks between 2350 cm^{-1} and 1900 cm^{-1} correspond to overtones of fundamental vibrations in the $1200\text{--}900\text{ cm}^{-1}$ region [43]. A detailed FTIR analysis was conducted to determine the species present in the synthetic mercury jarosite. Measurements of mass loss were also performed to propose the thermal decomposition stoichiometry. Therefore, the results from XRD and FTIR confirm that the mercury jarosite was successfully synthesized.

Table 2. FTIR spectral analysis of the synthetic mercury jarosite.

Spectral Band (cm^{-1})	Related Vibration	Spectral Band (cm^{-1})	Related Vibration
3310 vb	νOH	671 vw	$\nu_4\text{SO}_4^{2-}$
2350–1900 w, b	$2\nu\text{SO}_4^{2-}$, $2\delta\text{OH}^-$	636 w	$\nu_4\text{SO}_4^{2-}$
1630 w	$\delta\text{H}_2\text{O}$	618 m	Hg–O
1184 s	$\nu_3\text{SO}_4^{2-}$	563 sh	γOH^-
1087 s	$\nu_3\text{SO}_4^{2-}$	490 sh	$\nu\text{Fe-O}$, $\nu\text{Hg-O}$
1004 vs	δOH^-	465 s	$\nu\text{Fe-O}$, $\nu\text{Hg-O}$
996 sh	$\nu_1\text{SO}_4^{2-}$	430 s	$\nu_2\text{SO}_4^{2-}$

vb = very broad, b = broad, vs = very strong, s = strong, m = medium, w = weak, vw = very weak, sh = shoulder.

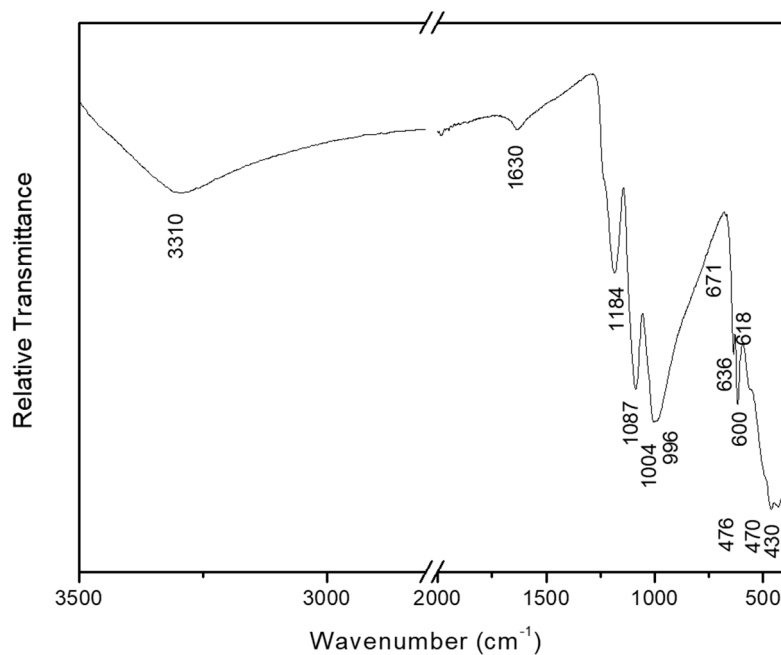


Figure 2. FTIR analysis of the synthetic mercury jarosite.

3.2. Thermal Characterization

Figure 3 shows the thermogravimetric analysis of the synthetic mercury jarosite. As can be seen, four mass loss stages were observed at 290 °C, 365 °C, 543 °C and 665 °C. The first mass loss stage (2.3%) observed from 120 °C to 320 °C corresponds to release of water retained by the sample, and the second one (7.2%)—at temperatures between 320 °C and 440 °C—is attributed to dehydroxylation. The third mass loss event relates to mercury loss due to decomposition into mercury oxide (16.1%), and the fourth stage is associated with sulfate loss (25.5%).

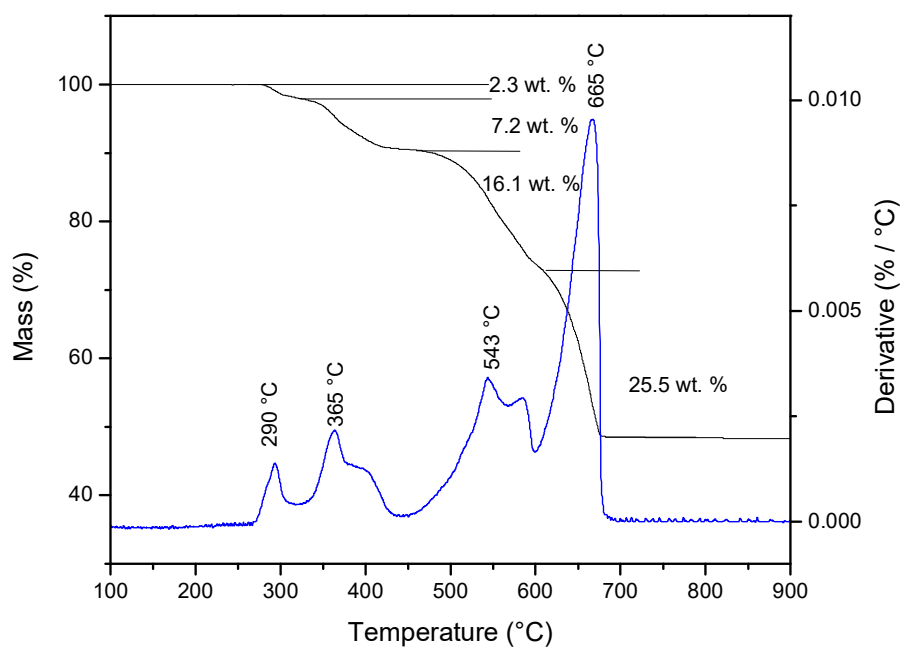


Figure 3. Thermogravimetric and derivative thermogravimetric analysis of Hg-jarosite.

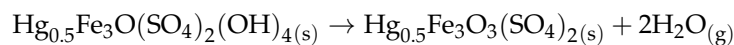
The following steps may explain the thermal decomposition mechanism of the synthetic mercury jarosite based on the theoretical formula, which are comprised of water loss being superficially retained

or contained in the compound's structure (first two steps), mercury loss (third step), and transformation and sulfur loss (fourth step).

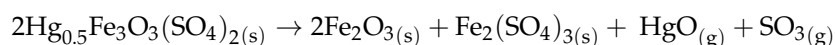
Step 1 (290 °C)



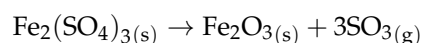
Step 2 (365 °C)



Step 3 (543 °C)



Step 4 (665 °C)



The hydronium content was not taken into account in the proposed mechanism, since it represents only about 7.1×10^{-3} wt. % of the total mass of the synthesized mercury jarosite (according to the presented formula), and therefore can be considered negligible. Frost et al. [37] reported that during the thermal decomposition of the hydronium jarosite, the loss of protons at 557 °C relates to the loss of H_2SO_4 , with further decomposition to produce SO_3 and H_2O .

Figures 4 and 5 show EDS and XRD results for the samples subjected to isothermal treatment, corresponding to each of the four thermal events observed in the thermogram. Signals of elements constituting the synthetic mercury jarosite (Fe, Hg, S, and O) are observed in Figure 4a,b, indicating that the weight loss in the first two stages relates to the loss of adsorbed and structural water, respectively. Results by XRD for the second stage show an amorphous compound, which contains S, Hg, Fe, and O, in addition to the mercury jarosite. XRD results after 400 °C-heat treatments show only low intense peaks from iron sulfate, indicating that the proposed phase $\text{Hg}_{0.5}\text{Fe}_3\text{O}_3(\text{SO}_4)_2$ at stage 2 is amorphous. Regarding the third stage, results from EDS show no evidence of Hg, only the presence of Fe, S, and O, indicating Hg sublimation (as HgO) and partial desulfurisation (Figure 4c). The corresponding XRD pattern provides evidence of the iron sulfate formation (Figure 5, 600 °C). Finally, EDS analysis shows the presence of Fe and O in the latter step (Figure 4d), which, according to the XRD results, correspond to the formation of hematite (Figure 5, 700 °C).

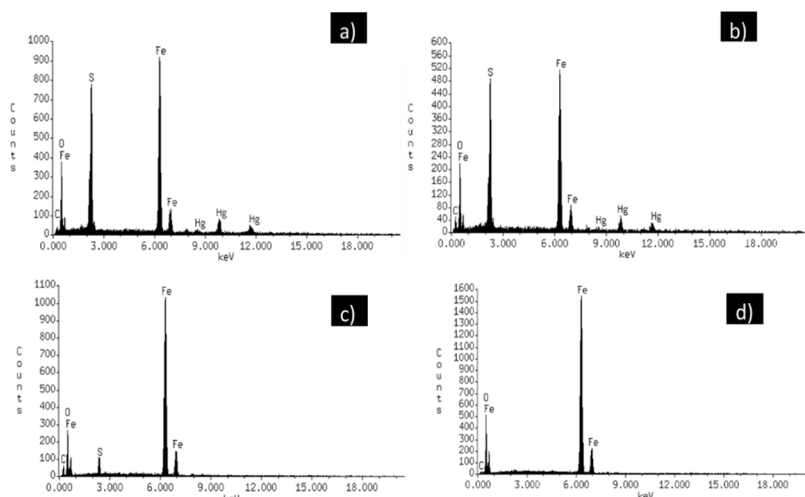


Figure 4. EDS analysis for isothermally treated samples at temperatures corresponding to each weight loss event: (a) first stage, (b) second stage, (c) third stage and (d) fourth stage.

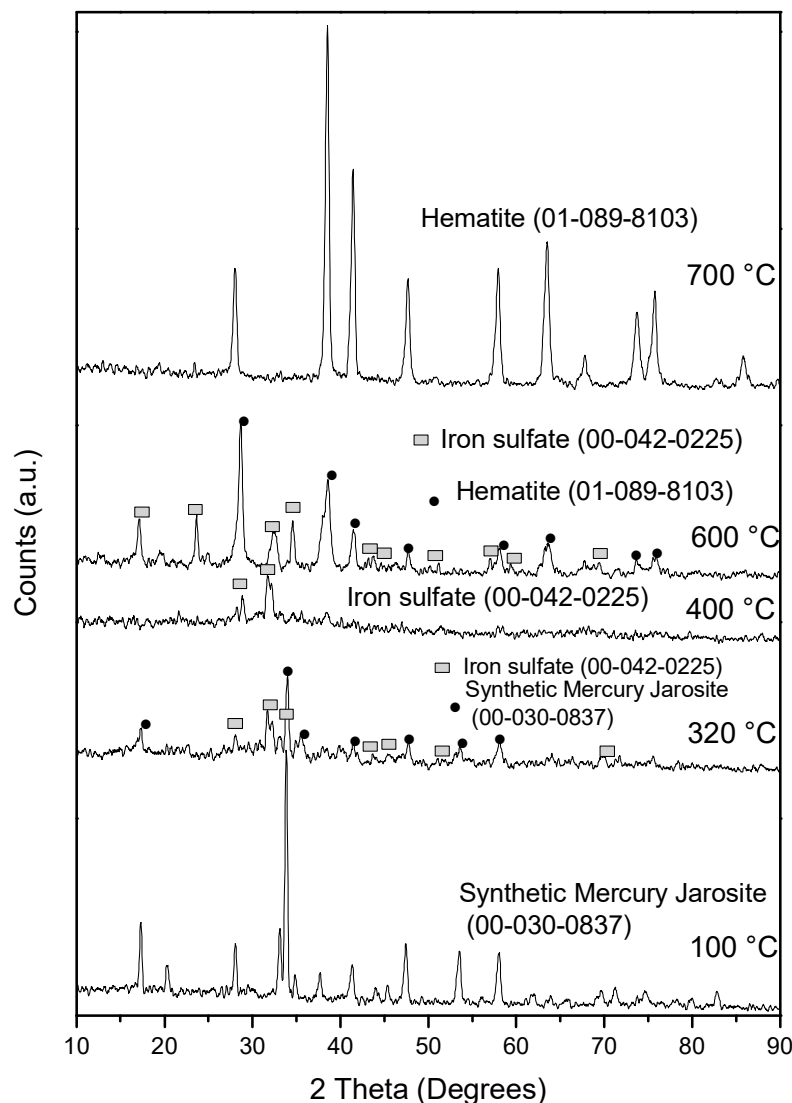


Figure 5. X-ray diffraction patterns of synthetic mercury jarosite and residues after calcination at different temperatures.

3.3. Kinetics of Thermal Decomposition

To obtain the remaining species in each decomposition stage, 1 g samples of synthetic mercury jarosite were first calcined for 1 h at 250 °C (for the first mass loss event), 350 °C (for the second stage), 510 °C (for the third stage), and 590 °C (for the fourth mass loss stage). To determine the activation energy corresponding to each of the four observed mass loss events, four samples from each calcined powder sample were subjected to isothermal treatments at 290 °C, 305 °C, 315 °C, and 325 °C for the first stage; 360 °C, 375 °C, 390 °C, and 400 °C for the second stage; 520 °C, 545 °C, 560 °C, and 590 °C for the third stage; and 600 °C, 620 °C, 635 °C, and 650 °C for the fourth stage.

Determination of kinetics requires calculation of the reacted material mass fraction according to Equation (1):

$$Y = \frac{(m_0 - m_t)}{(m_0 - m_f)} \quad (1)$$

where Y is the reacted mass fraction, m_0 is the initial mass, m_t is the mass at time t , and m_f is the mass at the end of the thermal decomposition process.

Once Y was calculated, the thermal dissociation of the synthetic mercury jarosite was plotted for each of the four stages as a function of time, as shown in Figure 6a–d.

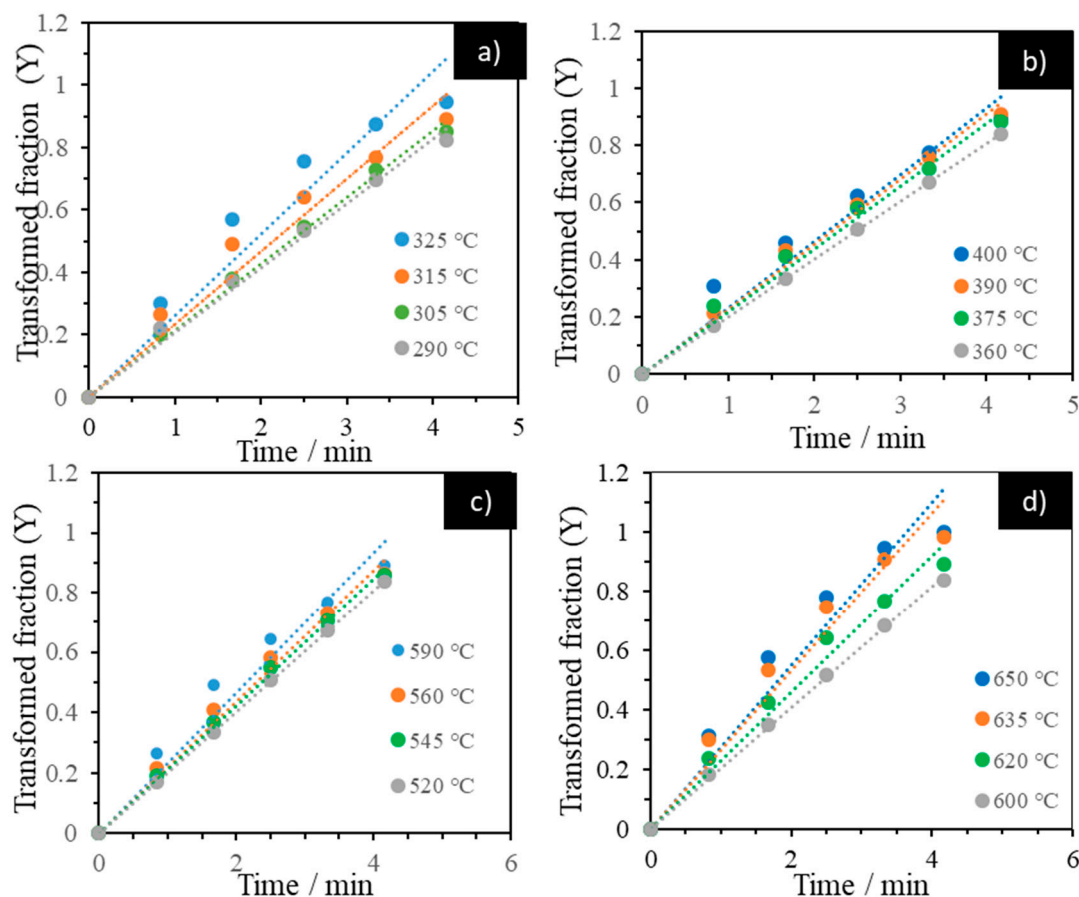


Figure 6. Reacted fraction of mercury jarosite obtained isothermally as function of time for the observed mass loss events: (a) first event, (b) second event, (c) third event, and (d) fourth event. The “time to given fraction” method relates t_Y to $Y = 0.5$ for each temperature.

The activation energy (E_a) can be estimated by the “time to given fraction” method, which considers that the transformed fraction and time (t) are functionally related. Therefore, t can be considered as the dependent variable instead of the rate constant (k), which is strongly dependent on T [46,47]. t_Y can be described by the expression:

$$t_Y = A^{-1} e^{\frac{E_a}{RT}} \quad (2)$$

Therefore,

$$\ln(t_Y) = -\ln A + \frac{E_a}{R} \times \frac{1}{T} \quad (3)$$

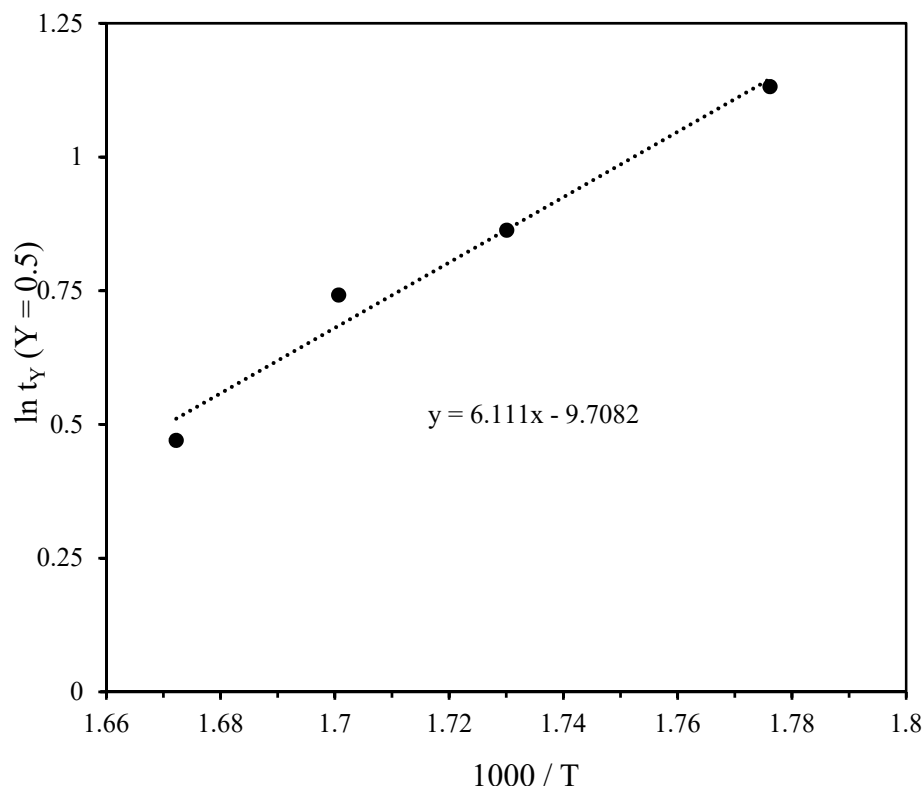
where time t_Y for a specific Y is determined from isothermal experiments (see Figure 6a–d). A in Equations (2) and (3) is a fitting constant, which relates to the number of collisions at the beginning of the reaction, R is the gas constant ($R = 8.3144 \times 10^{-3}$ kJ·mol $^{-1}$ ·K $^{-1}$), and T is temperature in K.

Table 3 summarizes the obtained t_Y values at fraction $Y = 0.5$ for each of the isothermal experiments conducted in the present work, along with the activation energy and the fitting constant obtained from the slope of the straight lines in Figures 7–10.

Table 3. Time taken to 50% of conversion ($Y = 0.5$) from the data obtained in Figure 6.

Stage	Time to 50%, t_Y (min)	$\ln(t_Y)$	Temperature (°C)	$1000/T$ (K $^{-1}$)	E_a (kJ·mol $^{-1}$)
First	3.1	1.13	290	1.77	50.80
	2.37	0.86	305	1.73	
	2.1	0.74	315	1.70	
	1.6	0.47	325	1.67	
Second	2.3	0.83	360	1.57	20.19
	2.1	0.74	375	1.54	
	2	0.69	390	1.50	
	1.8	0.58	400	1.48	
Third	2.3	0.83	520	1.26	44.80
	2.1	0.74	545	1.22	
	1.7	0.54	560	1.20	
	1.5	0.40	590	1.15	
Fourth	2.42	0.88	600	1.14	234.70
	1.45	0.37	620	1.11	
	1.03	0.03	635	1.10	
	0.38	-0.96	650	1.08	

The activation energy obtained for the first mass loss stage (Figure 7)— $E_a = 50.8$ kJ·mol $^{-1}$ —indicates that H₂O is adsorbed by strong hydrogen bonds to the jarosite structure, whilst dehydroxylation is a less temperature-dependent process, according to the low value obtained (20.19 kJ·mol $^{-1}$) for the activation energy corresponding to the second mass loss event (Figure 8). It has been claimed that dehydroxylation is controlled by a mixture of mass transport and temperature [48].

**Figure 7.** Arrhenius plot corresponding to the first mass loss event (retained water).

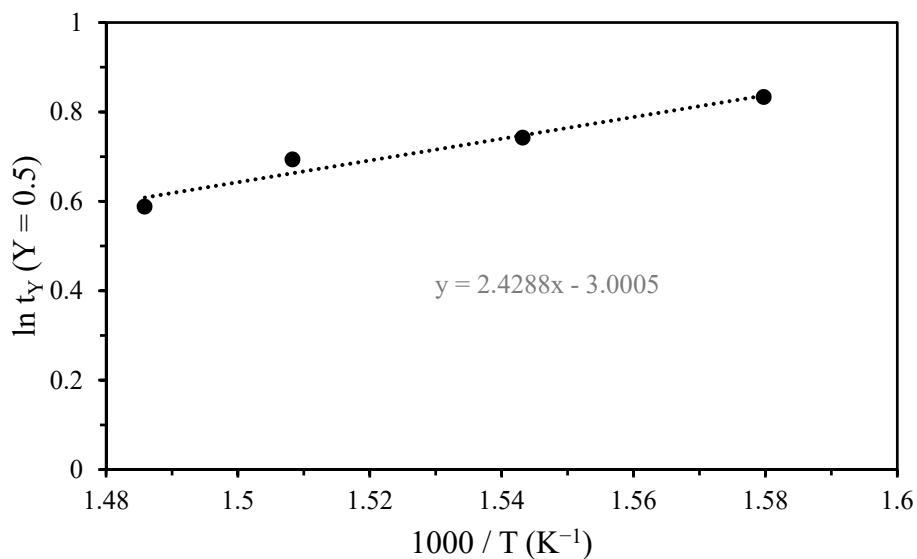


Figure 8. Arrhenius plot corresponding to the second mass t loss event (structural water).

The chemical reactions taking place in the third and fourth events are strongly dependent on temperature, as indicated by the high activation energy values obtained: $E_a = 44.8 \text{ kJ}\cdot\text{mol}^{-1}$ for the mercury sublimation and $E_a = 234.7 \text{ kJ}\cdot\text{mol}^{-1}$ for the thermal decomposition of the synthetic jarosite into hematite—which can be attributed to the high energy needed for breakage of S–O covalent bonds, resulting in the release of sulfur compounds. The high value of the calculated frequency factor ($A = 4.01 \times 10^{13}$ collisions) supports this observation.

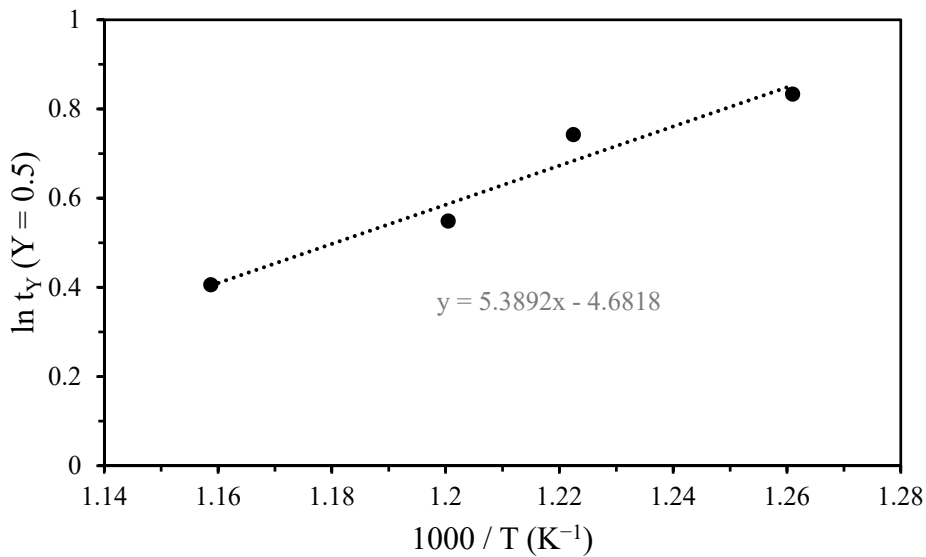


Figure 9. Arrhenius plot corresponding to the third mass t loss event (mercury sublimation).

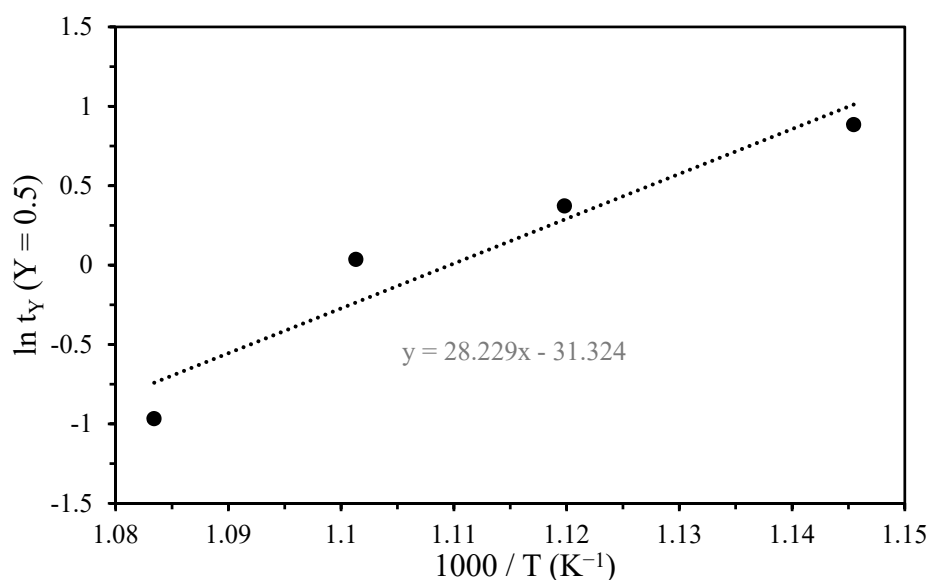


Figure 10. Arrhenius plot corresponding to the fourth mass t loss event (mercury sublimation).

4. Conclusions

The results by X-ray diffraction (ICDD-PDF 00-030-083) show that mercury jarosite was synthesized successfully. FTIR analysis shows the characteristic vibration modes of the Hg–O bond at 618 cm^{-1} , 490 cm^{-1} and 465 cm^{-1} . Thermogravimetric analyses show four weight losses: the first two attributed to adsorbed water and structural water (dehydroxylation), the third weight loss relates to transformation of mercury into different species and to desulfonization, and the fourth is associated with the sulfur loss due to the formation of different oxides. Results by EDS and XRD indicate that in all of the cases, hematite is the residual phase of the thermal decomposition process.

The activation energy calculated for each stage was 50.8 , 20.19 , 44.8 , and $234.7\text{ kJ}\cdot\text{mol}^{-1}$ for the first, second, third, and fourth loss mass events, respectively. These values indicate that weight loss events are controlled by temperature, with the exception of the dehydroxylation process which is controlled by mass transport (i.e., the resistance of reaction gas product through the laminar layer, limiting the rate of the process) and temperature. This later presents a mixed control, since the calculated activation energy is in the range of $20 \geq Ea \leq 40\text{ kJ}\cdot\text{mol}^{-1}$. A high energy is needed for decomposition of synthetic mercury jarosite, which means that they are stable compounds even at high temperatures and therefore, it is expected that mercury present in the jarosite is also stable. Results of the thermal analysis show that the synthetic mercury jarosites require higher decomposition temperature compared to other jarosite-type compounds—such those containing Pb, Na, H_3O , K, and NH_4 [36–38].

Author Contributions: M.U.F. performed the experimental work and wrote the first draft of the manuscript; I.A.R. conducted the thermal characterization; E.G.P. performed characterization by FTIR and SEM-EDS; F.P. helped in the interpretation and discussion of results; J.C.J. and M.R. performed kinetic analysis and characterization by XRD; A.M.T. conducted characterization by TGA and XRD; and H.I and E.J.G. reviewed and corrected the manuscript. All of the authors revised and approved the final version of the manuscript.

Funding: This research received no external funding.

Conflicts of Interest: The authors declare no conflict of interest.

References

1. Barringer, L.I.; Szabo, Z.; Kauffman, L.J.; Barringer, T.H.; Stackelberg, P.E.; Ivahnenko, T.; Rajagopalan, S.; Krabbenhoft, D.P. Mercury concentrations in water from an unconfined aquifer system, New Jersey coastal plain. *Sci. Total. Environ.* **2005**, *346*, 169–183. [[CrossRef](#)]
2. Borrell, A.; Aguilar, A.; Tornero, V.; Drago, M. Concentrations of mercury in tissues of striped dolphins suggest decline of pollution in Mediterranean open waters. *Chemosphere* **2014**, *107*, 319–323. [[CrossRef](#)]
3. Counter, S.A.; Buchanan, L.H. Mercury exposure in children: A review. *Toxicol. Appl. Pharmacol.* **2004**, *198*, 209–230. [[CrossRef](#)]
4. Maurice-Bourgois, L.; Quiroga, I.; Chincheros, J.; Courau, P. Mercury distribution in waters and fishes of the upper Madeira rivers and mercury exposure in riparian Amazonian populations. *Sci. Total. Environ.* **2000**, *260*, 73–86. [[CrossRef](#)]
5. Crespo, M.E.; Macedo, G.L.; Pereira, S.I.D.; Arrifano, G.P.F.; Picanço, D.L.W.; Do Nascimento, J.L.M.; Herculano, A.M. Mercury and human genotoxicity: Critical considerations and possible molecular mechanisms. *Pharmacol. Res.* **2009**, *60*, 212–220. [[CrossRef](#)]
6. Qiu, G.; Feng, X.; Wang, S.; Shang, L. Mercury and methylmercury in riparian soil, sediments, mine-waste calcines, and moss from abandoned Hg mines in east Guizhou province, southwestern China. *Appl. Geochem.* **2005**, *20*, 627–638. [[CrossRef](#)]
7. Feng, X.; Li, P.; Qiu, G.; Wang, S.; Li, G.; Shang, L.; Meng, B.; Jiang, H.; Bai, W.; Li, Z. Human exposure to methylmercury through rice intake in mercury mining areas, Guizhou Province, China. *Environ. Sci. Technol.* **2007**, *42*, 326–332. [[CrossRef](#)]
8. Qiu, G.; Feng, X.; Wang, S.; Shang, L. Environmental contamination of mercury from Hg-mining areas in Wuchuan, northeastern Guizhou, China. *Environ. Pollut.* **2006**, *142*, 549–558. [[CrossRef](#)]
9. Li, G.H.; Feng, X.B.; Qiu, G.L.; Bi, X.Y.; Li, Z.G.; Zhang, C.; Wang, D.Y.; Shang, L.H.; Guo, Y.N. Environmental mercury contamination of an artisanal zinc smelting area in Weining County, Guizhou, China. *Environ. Pollut.* **2008**, *154*, 21–31. [[CrossRef](#)]
10. Garcia, A.; Murciego, A.; Alvarez, E.; Regina, I.S.; Rodriguez, M. Mercury in soils and plants in an abandoned cinnabar mining area (SW Spain). *J. Hazard. Mater.* **2009**, *68*, 1319–1324. [[CrossRef](#)]
11. Pataranawat, P.; Parkpian, P.; Polprasert, C.; Delaune, R.; Jugsujinda, A. Mercury emission and distribution: Potential environmental risks at a small-scale gold mining operation, Phichit Province, Thailand. *J. Environ. Sci. Health A Tox. Hazard. Subst. Environ. Eng.* **2007**, *42*, 1081–1093. [[CrossRef](#)]
12. Egler, S.G.; Rodrigues, S.; Villas, R.C.; Beinhoff, C. Evaluation of mercury pollution in cultivated and wild plants from two small communities of the Tapajos gold mining reserve, Para State, Brazil. *Sci. Total Environ.* **2006**, *368*, 424–433. [[CrossRef](#)]
13. Rieuwerts, J.S.; Farago, M. Mercury concentrations in a historic lead mining and smelting town in the Czech Republic: A pilot study. *Sci. Total Environ.* **1996**, *188*, 167–171. [[CrossRef](#)]
14. Wang, J.; Feng, X.; Anderson, C.W.N.; Xingd, Y.; Shanga, L. Remediation of mercury contaminated sites —A review. *J. Hazard. Mater.* **2012**, *221*, 1–18. [[CrossRef](#)]
15. Southworth, G.; Lindberg, S.; Zhang, H.; Anscombe, F. Fugitive mercury emissions from a chlor-alkali factory: Sources and fluxes to the atmosphere. *Atmos. Environ.* **2004**, *38*, 597–611. [[CrossRef](#)]
16. Semu, E.; Singh, B.R.; Selmer-Olsen, A.R. Adsorption of mercury compounds by tropical soils II. Effect of soil: Solution ratio, ionic strength, pH, and organic matter. *Water Air Soil Pollut.* **1987**, *32*, 1–10. [[CrossRef](#)]
17. Cheng, H.; Hu, Y. Mercury in municipal solid waste in China and its control: A review. *Environ. Sci. Technol.* **2012**, *46*, 593–605. [[CrossRef](#)]
18. Liu, J.; Valsaraj, K.T.; Devai, I.; DeLaune, R. Immobilization of aqueous Hg (II) by mackinawite (FeS). *J. Hazard. Mater.* **2008**, *157*, 432–440. [[CrossRef](#)] [[PubMed](#)]
19. Zhang, R.H.; Sun, H.W.; Yan, Q.S.; Sun, H.F. Laboratory study on remediation of mercury contaminated soil by iron chips. *Ecol. Environ.* **2007**, *16*, 437–441. (In Chinese)
20. Backstrom, M.; Dario, M.; Karlsson, S.; Allard, B. Effects of a fulvic acid on the adsorption of mercury and cadmium on goethite. *Sci. Total Environ.* **2003**, *304*, 257–268. [[CrossRef](#)]
21. Meng, X.; Hua, Z.; Dermatas, D.; Wang, W. Immobilization of mercury (II) in contaminated soil with used tire rubber. *J. Hazard. Mater.* **1998**, *57*, 231–241. [[CrossRef](#)]

22. Hovsepyan, A.; Bonzongo, J.C.J. Aluminum drinking water treatment residuals (Al-WTRs) as sorbent for mercury: Implications for soil remediation. *J. Hazard. Mater.* **2009**, *164*, 73–80. [[CrossRef](#)]
23. Mulligan, C.N.; Yong, R.N.; Gibbs, B.F. An evaluation of technologies for the heavy metal remediation of dredged sediments. *J. Hazard. Mater.* **2001**, *85*, 145–163. [[CrossRef](#)]
24. Xiong, Z.; He, F.; Zhao, D.; Barnett, M.O. Immobilization of mercury in sediment using stabilized iron sulfide nanoparticles. *Water Res.* **2009**, *43*, 5171–5179. [[CrossRef](#)]
25. Tungittiplakorn, W.; Cohen, C.; Leonard, W. Engineered polymeric nanoparticles for bioremediation of hydrophobic contaminants. *Environ. Sci. Technol.* **2005**, *39*, 1354–1358. [[CrossRef](#)]
26. Dutrizac, J.E.; Jambor, J.L. Jarosites and their application in hydrometallurgy. *Rev. Mineral. Geochem.* **2000**, *40*, 405–452. [[CrossRef](#)]
27. Buckby, T.; Black, S.; Coleman, M.L.; Hodson, M.E. Fe-sulphate-rich evaporative mineral precipitates from the Rio Tinto, southwest Spain. *Mineral. Mag.* **2003**, *67*, 263–278. [[CrossRef](#)]
28. Das, G.K.; Anand, S.; Acharya, S.; Das, R.P. Preparation and decomposition of ammoniojarosite at elevated temperatures in $H_2O-(NH_4)_2SO_4-H_2SO_4$ media. *Hydrometallurgy* **1995**, *38*, 263–276. [[CrossRef](#)]
29. Patiño, F.; Flores, M.U.; Reyes, I.A.; Reyes, M.; Hernández, J.; Rivera, I.; Juárez, J.C. Alkaline decomposition of synthetic jarosite with arsenic. *Geochem. Trans.* **2013**, *14*, 2. [[CrossRef](#)] [[PubMed](#)]
30. Patiño, F.; Reyes, I.A.; Flores, M.U.; Pandiyan, T.; Roca, A.; Reyes, M.; Hernández, J. Kinetic modeling and experimental design of the sodium arsenojarosite decomposition in alkaline media: Implications. *Hydrometallurgy* **2013**, *137*, 115–125. [[CrossRef](#)]
31. Flores, M.U.; Patiño, F.; Reyes, I.A.; Reyes, M.; Rivera, I.; Juárez, J.C. Kinetic modeling of the alkaline decomposition of potassium arsenojarosite. *J. Braz. Chem. Soc.* **2012**, *23*, 1018–1023. [[CrossRef](#)]
32. Reyes, I.A.; Patiño, F.; Rivera, I.; Flores, M.U.; Reyes, M.; Hernández, J. Alkaline reactivity of arsenical natrojarosite. *J. Braz. Chem. Soc.* **2012**, *22*, 2260–2267. [[CrossRef](#)]
33. Asta, M.P.; Cama, J.; Martínez, M.; Giménez, J. Arsenic removal by goethite and jarosite in acidic conditions and its environmental implications. *J. Hazard. Mater.* **2009**, *171*, 965–972. [[CrossRef](#)] [[PubMed](#)]
34. Dutrizac, J.E.; Kaiman, S. Synthesis and properties of jarosite-type compounds. *Can. Mineral.* **1976**, *14*, 151–158.
35. Dutrizac, J.E.; Chen, T.T. The synthesis of mercury jarosite and the mercury concentration in jarosite-family minerals. *Can. Mineral.* **1981**, *19*, 550–569.
36. Frost, R.L.; Weier, M.L.; Martens, W. Thermal decomposition of jarosites of potassium, sodium and lead. *J. Therm. Anal. Calorim.* **2005**, *82*, 115–118. [[CrossRef](#)]
37. Frost, R.L.; Wills, R.A.; Kloprogge, J.T.; Materns, W.N. Thermal decomposition of hydronium jarosite (H_3O) $Fe_3(SO_4)_2(OH)_6$. *J. Therm. Anal. Calorim.* **2006**, *83*, 213–218. [[CrossRef](#)]
38. Frost, R.L.; Wills, R.A.; Kloprogge, J.T.; Materns, W. Thermal decomposition of ammonium jarosite (NH_4) $Fe_3(SO_4)_2(OH)_6$. *J. Therm. Anal. Calorim.* **2006**, *84*, 489–496. [[CrossRef](#)]
39. Ordoñez, S.; Patiño, F.; Reyes, I.A.; Flores, M.U.; Flores, V.H.; Palacios, E.G.; Reyes, M. Synthesis and topology of the reaction of mercury jarosite in NaOH medium. In Proceedings of the European Metallurgical Conference, Duesseldorf, Germany, 14–17 June 2015; Volume 1, pp. 537–552.
40. Jeffery, G.H.; Bassett, J.; Mendham, J.; Denney, R.C. *Vogel's, Textbook of Quantitative Chemical Analysis*; Longman Scientific and Technical: London, UK, 1989.
41. Askarinejad, A.; Morsali, A. Synthesis and characterization of mercury oxide unusual nanostructures by ultrasonic method. *Chem. Eng. J.* **2009**, *153*, 183–186. [[CrossRef](#)]
42. Xhaxhiu, K.; Saraci, E.; Bente, K. Sequestration of supercritical CO₂ by mercury oxide. *Chem. Pap.* **2013**, *67*, 594–600. [[CrossRef](#)]
43. Refat, M.S.; Elsabawy, K.M. Infrared spectra, Raman laser, XRD, DSC/TGA and SEM investigations on the preparations of selenium metal, (Sb₂O₃, Ga₂O₃, SnO and HgO) oxides and lead carbonate with pure grade using acetamide precursors. *Bull. Mater. Sci.* **2011**, *34*, 873–881. [[CrossRef](#)]
44. Bishop, J.L.; Murad, E. The visible and infrared spectral properties of jarosite and alunite. *Am. Mineral.* **2005**, *90*, 1100–1107. [[CrossRef](#)]
45. Sasaki, K.; Tanaike, O.; Konno, H. Distinction of jarosite-group compounds by Raman spectroscopy. *Can. Mineral.* **1998**, *36*, 1225–1235.
46. Jiménez, A.; Prieto, M. Thermal stability of ettringite exposed to atmosphere: Implications for the uptake of harmful ions by cement. *Environ. Sci. Technol.* **2015**, *49*, 7957–7964. [[CrossRef](#)]

47. Putnis, A. *Introduction to Mineral Sciences*; Cambridge University Press: Cambridge, UK, 1992.
48. Ballester, A.; Felipe Verdeja, L.; Sancho, J. *Metalurgia Extractiva*, 2nd ed.; Síntesis: Barcelona, Spain, 2000; Volume I.



© 2019 by the authors. Licensee MDPI, Basel, Switzerland. This article is an open access article distributed under the terms and conditions of the Creative Commons Attribution (CC BY) license (<http://creativecommons.org/licenses/by/4.0/>).